



## Small Magellanic Cloud Cepheids Observed with the Hubble Space Telescope Provide a New Anchor for the SH0ES Distance Ladder

LOUISE BREUVAL <sup>1</sup>, ADAM G. RIESS <sup>1,2</sup>, STEFANO CASERTANO,<sup>2</sup> WENLONG YUAN <sup>1</sup>, LUCAS M. MACRI <sup>3</sup>,  
MARTINO ROMANIELLO <sup>4</sup>, YUKEI S. MURAKAMI <sup>1</sup>, DANIEL SCOLNIC <sup>5</sup>, GAGANDEEP S. ANAND <sup>2</sup>, AND  
IGOR SOSZYŃSKI <sup>6</sup>

<sup>1</sup>*Department of Physics and Astronomy, Johns Hopkins University, Baltimore, MD 21218, USA*

<sup>2</sup>*Space Telescope Science Institute, 3700 San Martin Drive, Baltimore, MD 21218, USA*

<sup>3</sup>*NSF's NOIRLab, 950 N Cherry Ave, Tucson AZ 85719, USA*

<sup>4</sup>*European Southern Observatory, Karl-Schwarzschild-Strasse 2, 85478 Garching bei München, Germany*

<sup>5</sup>*Department of Physics, Duke University, Durham, NC 27708, USA*

<sup>6</sup>*Astronomical Observatory, University of Warsaw, Al. Ujazdowskie 4, 00-478 Warszawa, Poland*

### ABSTRACT

We present photometric measurements of 88 Cepheid variables in the core of the Small Magellanic Cloud (SMC), the first sample obtained with the *Hubble* Space Telescope (*HST*) and Wide Field Camera 3, in the same homogeneous photometric system as past measurements of all Cepheids on the SH0ES distance ladder. We limit the sample to the inner core and model the geometry to reduce errors in prior studies due to the non-trivial depth of this Cloud. Without crowding present in ground-based studies, we obtain an unprecedentedly low dispersion of 0.102 mag for a Period-Luminosity relation in the SMC, approaching the width of the Cepheid instability strip. The new geometric distance to 15 late-type detached eclipsing binaries in the SMC offers a rare opportunity to improve the foundation of the distance ladder, increasing the number of calibrating galaxies from three to four. With the SMC as the only anchor, we find  $H_0 = 74.1 \pm 2.1 \text{ km s}^{-1} \text{ Mpc}^{-1}$ . Combining these four geometric distances with our *HST* photometry of SMC Cepheids, we obtain  $H_0 = 73.17 \pm 0.86 \text{ km s}^{-1} \text{ Mpc}^{-1}$ . By including the SMC in the distance ladder, we also double the range where the metallicity ([Fe/H]) dependence of the Cepheid Period-Luminosity relation can be calibrated, and we find  $\gamma = -0.22 \pm 0.05 \text{ mag dex}^{-1}$ . Our local measurement of  $H_0$  based on Cepheids and Type Ia supernovae shows a  $5.8\sigma$  tension with the value inferred from the CMB assuming a  $\Lambda$ CDM cosmology, reinforcing the possibility of physics beyond  $\Lambda$ CDM.

### 1. INTRODUCTION

The tension between the local measurement of the Hubble constant ( $H_0$ ) based on distances and redshifts (e.g.,  $H_0 = 73.0 \pm 1.0 \text{ km s}^{-1} \text{ Mpc}^{-1}$  Riess et al. 2022a) and its value inferred from the  $\Lambda$ CDM model calibrated with CMB data in the early universe (e.g.,  $H_0 = 67.4 \pm 0.5 \text{ km s}^{-1} \text{ Mpc}^{-1}$  Planck Collaboration et al. 2020) has reached a  $5\sigma$  significance. Extensive, recent reviews of the measurements are provided by Di Valentino et al. (2021) and Verde et al. (2023). This intriguing discrepancy provides growing hints of new physics beyond  $\Lambda$ CDM, which might include exotic dark energy, new relativistic particles, neutrino interactions or a small cur-

vature. Continued efforts to test  $\Lambda$ CDM in the late and early Universe to identify departures and tensions are warranted. While this tension is well-documented, increasing the number of calibrations or anchors of the local distance measurements is of great importance in order to better characterize and quantify the size of the tension.

Cepheid variables have been the “gold standard” of primary distance indicators for over a century. They are well-understood pulsating stars (Eddington 1917) and are easy to identify thanks to their large amplitude light curves at optical wavelengths. The Cepheids in the Small Magellanic Cloud (SMC) in particular played a foundational role in the recognition of their use as distance indicators and subsequent application to the discoveries of extragalactic nature of galaxies and the

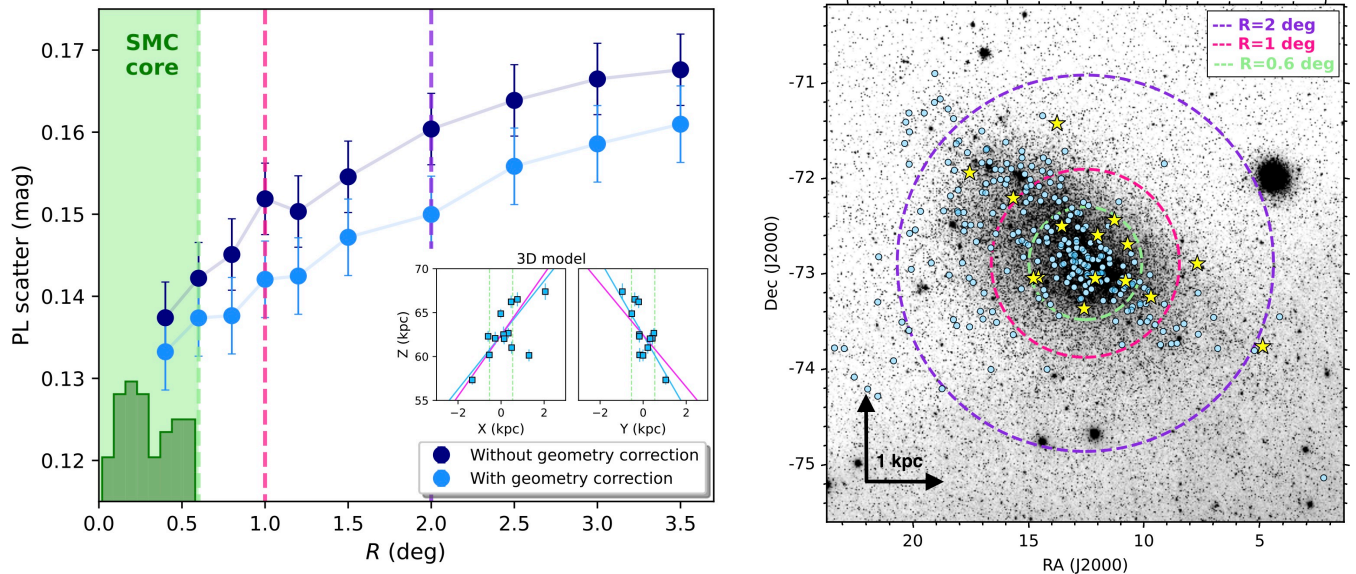


**Figure 1.** (Left): P–L scatter in the NIR  $W_{JK}$  Wesenheit index for different Cepheid subsamples located at increasing distances from the SMC center. For this test, Cepheid photometry was taken from the ground-based survey of Ripepi et al. (2017) and the geometric corrections were derived using the planar geometry by Graczyk et al. (2020). The green histogram in the bottom left corner shows the distribution of our Cepheid sample. The small inset on the right shows the position of DEBs from Graczyk et al. (2020) on the XZ and YZ planes, with the blue and pink lines showing the model fits from DEBs and from our Cepheid sample respectively. (Right): Map of SMC Cepheids from Ripepi et al. (2017) in light blue with the regions corresponding to radii of 2 deg, 1 deg and 0.6 deg. Eclipsing binaries from Graczyk et al. (2020) are shown in yellow.

expansion of the Universe (Hubble 1929). In the early 1900s, Henrietta Leavitt discovered a remarkable phenomenon by examining photographic plates of the SMC: Cepheids brightness follow a linear relationship with the logarithm of their period, with the brightest Cepheids having the longest periods. This law is now called the Leavitt law (Leavitt & Pickering 1912) or simply the Period-Luminosity (P–L) relation.

Since this discovery, SMC Cepheids have been used extensively to map the structure of this galaxy (Scowcroft et al. 2016; Jacyszyn-Dobrzyniecka et al. 2016), to investigate possible non-linearities in the P–L relation (Sandage et al. 2009), to study the chemical composition of these pulsating stars (Lemasle et al. 2017), or to calibrate the Cepheid metallicity dependence (Wielgórski et al. 2017; Gieren et al. 2018; Breuval et al. 2021, 2022). SMC Cepheids have been observed by large surveys, and complete light curves have been obtained at multiple wavelengths (Soszyński et al. 2015; Scowcroft et al. 2016; Ripepi et al. 2017; Gaia Collaboration et al. 2021). As a nearby dwarf galaxy and a direct neighbor of the Milky Way, the SMC is a great laboratory for many astrophysical studies. However, the downside of this galaxy, in particular for distance measurements, is its elongated shape along the line of sight which produces a detectable range of 5–10% in the distances to its stars. The consequence is that SMC Cepheids show a higher

scatter than their LMC cousins. However, it is possible to reduce the variation in depth by limiting studies to the SMC core (rather than the far-flung streams and condensations that surround it) and by the application of a geometric model recently derived from a study of the detached eclipsing binaries (DEBs) near the core as shown in Fig. 1; the Cepheid dispersion is reduced if a geometric model fit to the DEBs is applied (light blue vs. dark blue points in Fig. 1). The geometric correction assumed here is based on a planar geometry, such as the one from Graczyk et al. (2020). In the past, these corrections have been often neglected, resulting in a large scatter and even a bias in the P–L intercept and in the metallicity dependence (Wielgórski et al. 2017; Owens et al. 2022); see also the discussion in Breuval et al. (2022). By limiting to the core and accounting for the depth, ground-based NIR samples produce a P–L scatter of  $\sim 0.13$  mag, approaching the state-of-the-art.

The new geometric distance to the SMC by Graczyk et al. (2020), based on late-type DEBs, provides a unique opportunity to improve the distance ladder by increasing the number of anchor galaxies from three to four. One of the strengths of the SH0ES distance ladder is in the consistency of the photometric measurements across all of the first and second rungs: *all* Cepheid photometry is obtained in a single homogeneous photometric system with the *Hubble* Space Telescope (*HST*) Wide

Field Camera 3 (WFC3), the only instrument capable of reaching Cepheids in SNe Ia hosts as well as observing nearby Cepheids in the Milky Way, therefore cancelling zero-point errors. Indeed, combining ground-based and *HST* photometry would likely produce a 1.4–1.8% systematic error in the measured distances simply due to bandpass differences (Riess et al. 2019a). Also, due to the density of stars in the SMC core, typical ground-based samples with seeing worse than an arc second suffer from crowding. Because of the lack of *HST* photometry in the same system, the SMC could not be previously included as an anchor of the SH0ES distance ladder for calibrating Cepheids (Riess et al. 2022a). In order to make full use of the new geometric distance to the SMC, we observed a sample of Cepheids in the core of the SMC to mitigate the depth effects, using *HST* resolution instead of ground-based photometry to avoid crowding, and in the same photometric system (*HST*/WFC3) used for the SH0ES distance ladder to ensure consistency and negate photometric zero-points. As we show, these further reduce the scatter to a best-seen 0.10 mag while putting all Cepheids on the same photometric system as the rest of the distance ladder.

We describe our observations in §2 and the Cepheid photometry and phase corrections in §3. The P–L relations, as well as a discussion of the effects of metallicity and of the SMC geometry, are presented in §4. The Hubble constant is derived in §5 from our *HST* photometry and the previous SH0ES data. Finally, we discuss the results and prospects for  $H_0$  in §6.

## 2. OBSERVATIONS

### 2.1. Sample selection

The data used in this paper were obtained as part of the *HST* Cycle 30 program GO-17097 (PI: A. Riess) between 2023 June 23 and October 4. We selected our sample based on the OGLE-IV catalog of Magellanic Cloud Cepheids (Soszyński et al. 2015). To decrease depth effects and to reduce the P–L scatter (Fig. 1), we excluded Cepheids beyond 0.6 deg from the SMC center ( $\alpha = 12.54$  deg,  $\delta = -73.11$  deg, from Ripepi et al. 2017). This region is small enough to mitigate the depth effects and contains enough Cepheids to populate the P–L relation. We discuss the effects of the SMC geometry in §4.2. Finally, we selected Cepheids in the range  $0.7 < \log P < 2.0$ , with  $P$  the pulsation period in days, similar to Riess et al. (2019a) in the LMC, to avoid contamination from shorter period overtone Cepheids ( $\sim 46\%$  of all SMC Cepheids) and possible non-linearities in the P–L relation at shorter periods.

### 2.2. The DASH mode

Because the SMC is a very nearby galaxy, the mean separation between Cepheids is large ( $\sim 12'$ ) compared to the WFC3 field of view ( $\sim 2.5'$ ). It is therefore inefficient to observe SMC Cepheids individually with *HST* using normal pointing procedures, which require  $\sim 6-7$  minutes for a guide star lock every time a new position is acquired. However, the rapid-exposure observing mode of *HST* called “DASH” (Drift And SHift; Momcheva et al. 2017), available since Cycle 24, makes the observations much more efficient than the classic procedure by slewing the telescope a few arcminutes between Cepheid pairs under gyroscope control, allowing us to observe multiple short-exposure targets in a single orbit after a single guide star acquisition. This technique was successfully adopted by Riess et al. (2019a), hereafter R19, to observe 70 LMC Cepheids (GO-14648, GO-15145), which enabled the use of this galaxy as a primary anchor of the distance ladder. In the following, we adopt the approach from R19 to ensure consistency between Cepheid measurements in both galaxies and to negate systematic uncertainties in the photometry.

We selected 15 sequences of 6 or 7 Cepheids such that the slewing of the telescope was minimized, as shown in the right panel of Fig. 2. The length of each sequence was chosen so that each could be observed during one *HST* visibility period, typically  $\sim 2.5$  ksec. For a given sequence, we first observed each Cepheid in the NIR  $F160W$  filter, then flipped the WFC3 mirror mechanism and reversed the path to observe them in UVIS filters  $F555W$  and  $F814W$ . To avoid the loss of efficiency that would be caused by a memory dump, we used subarrays instead of full frame images. We started with  $33''$  subarrays in the NIR ( $256 \times 256$  pixels, IRSUB256), then  $40''$  subarrays in the first optical exposures ( $1K \times 1K$  pixels, C1K1C) and larger  $80''$  subarrays ( $2K \times 2K$  pixels, 2K2C) for the last optical images. This successive expansion of the array size was intended to keep the target in the field of view even with a gyro drift rate of up to twice the expected value.

The first observation (visit 12) was obtained successfully on 2023 June 23 with an accumulated drift of  $15''$  by the end of the visit, keeping all Cepheids well within the subarrays and providing images of 7 targets in 3 filters. The following visits, observed between 2023 August 10-16, were severely affected by a period of erratic performance of gyro 3, causing large drifts up to ten times larger than expected, placing most Cepheids outside the frame.

After a number of missed targets, we adopted a new strategy and redesigned subsequent and repeat observations to complete the exposures in the missing filters

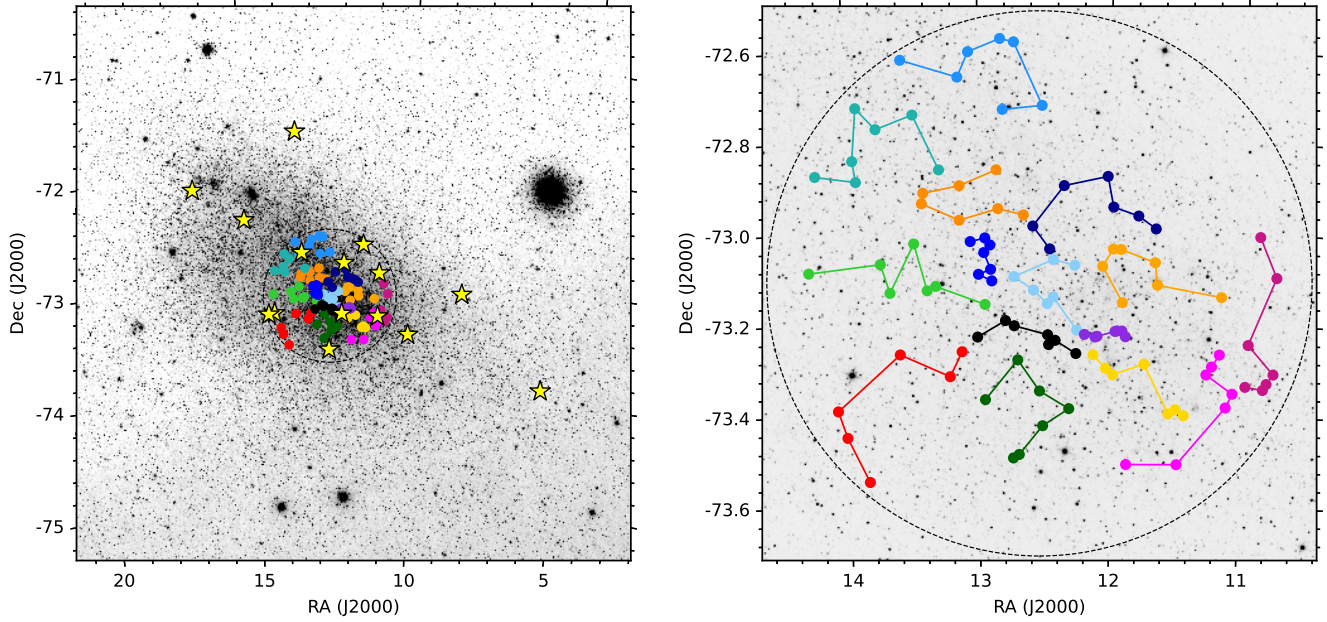


**Figure 2. (Left):** The dashed circle shows the core region of the SMC ( $R = 0.6$  deg). Detached eclipsing binaries from Graczyk et al. (2020) are shown in yellow and the colored dots are the Cepheids from the present study. **(Right):** Zoom-in of the SMC core region. The 15 Cepheid sequences (one per *HST* orbit) are shown in color.

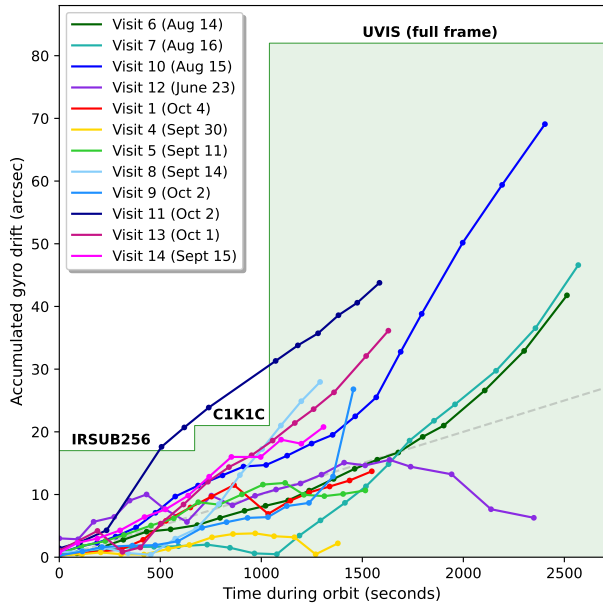


**Figure 3.** Accumulated drift of the pointing due to the gyroscopic control in the “DASH” mode of *HST*. The green region shows the size of the image (with the subarray names) and the dashed grey line is the expected drift of  $0.01''/\text{sec}$  (STScI handbook). Visits 2, 3 and 15 were observed under FGS control and therefore are not shown in this figure. The failed visits observed in the first attempt (with drifts up to  $200''$ ) are not represented in this figure.

and to allow for a greater drift. For the visits that completely failed (gyro drift larger than the array size in the first two exposures), we repeated the observations with full frame images ( $\text{BIN}=2$ ) for the last third of the orbit to accommodate larger drifts. These full frame images require more memory, thus we were only able to fit 5 targets per orbit. For the visits that had partial success (some Cepheids were observed but not in all three filters), we repeated only the missed filters under Fine Guidance Sensor (FGS) control, independent of the gyro behavior. In this configuration, we were able to fit 4 targets per orbit. In some cases, the images were large enough to observe two very nearby Cepheids in the same frame. The 7 rescoped visits were successfully executed between 2023 September 11 and October 4. Our final sample comprises 88 Cepheids (out of the 104 proposed), representing only a net 9% loss in the statistical power of the sample.

The accumulated drift caused by the gyroscope guiding is plotted as a function of time during each orbit in Fig. 3. With a typical accumulated drift of  $30''$  at the end of a visit (2.5 ksec), we expect the Cepheid flux to be smeared by 0.7 pixel ( $0.03''$ ) at most during a 2.5-second exposure on the UVIS detector, which we can accommodate with a large photometric aperture. Due to the gyroscope control, Cepheids are often located far from the center of the images and their coordinates are incorrect (in this mode, *HST* cannot use the astrometry

**Table 1.** Observations of SMC Cepheids

Cepheid	Frame	Filter	MJD (days)	Exposure time (s)	Array	X <sub>Cepheid</sub>	Y <sub>Cepheid</sub>
						(pixels)	
OGLE-0518	iev9tuh3q	F160W	60218.482	2.50	IRSUB256	138.4	129.2
OGLE-0518	iev9tuhcq	F555W	60218.490	2.50	UVIS1	843.2	680.8
OGLE-0518	iev9tuhdq	F814W	60218.492	2.50	UVIS1	817.8	706.1
OGLE-0524	iev9tuh4q	F160W	60218.483	2.50	IRSUB256	126.2	142.0
OGLE-0524	iev9tuhbq	F555W	60218.489	2.50	UVIS2-C1K1C-SUB	195.5	796.1
OGLE-0524	iev9tuhaq	F814W	60218.488	2.50	UVIS2-C1K1C-SUB	231.3	761.5
OGLE-0524	iev9tuh4q	F160W	60218.483	2.50	IRSUB256	126.2	142.0
OGLE-0524	iev9tuhbq	F555W	60218.489	2.50	UVIS2-C1K1C-SUB	195.5	796.1
OGLE-0524	iev9tuhaq	F814W	60218.488	2.50	UVIS2-C1K1C-SUB	231.3	761.5
OGLE-0541	iev9tuh1q	F160W	60218.478	2.50	IRSUB256	130.7	141.8
OGLE-0541	iev9tuhgq	F555W	60218.496	2.50	UVIS1	720.8	808.3
OGLE-0541	iev9tuhhq	F814W	60218.497	2.50	UVIS1	683.9	845.0

**Notes:** (\*) Indicates a drift rate larger than 0.08'' during the exposure necessitating a larger photometry aperture.

(This table is available in its entirety in machine-readable form.)

of a guide star to establish the pointing coordinates). We therefore used the positions of the brightest stars from the *Gaia* DR3 catalog (Gaia Collaboration et al. 2021) to identify the Cepheid in each image. For some of the observations with the largest drifts, direct position matching was not sufficient; in such cases we used a histogram-based algorithm to match source positions to the *Gaia* catalog. This algorithm is robust to the presence of outliers, e.g., due to cosmic rays, and works up to offsets well over 10'. This method allowed us to estimate drifts from the intended pointing that in some cases exceeded several arcminutes. However, none of the successful observations required this approach. The observations are described in Table 1.

### 3. SMC CEPHEID PHOTOMETRY

#### 3.1. Aperture photometry

In this section we describe the procedure to measure the flux associated to each Cepheid in the three filters. To accommodate for possible variations in the PSF due to gyro drifts, we perform aperture photometry following the approach described in R19. We measured the photometry in ‘‘FLC’’ files in the optical, which are corrected for the charge transfer efficiency (CTE), and ‘‘FLT’’ files in the NIR. The images were multiplied by pixel area maps to account for the different on-sky pixel size across the field of view. In the case of UVIS full frame images (2×2 binned), we constructed and applied a 2×2 binned pixel area map.

For most images, we use a photometric aperture with radius of 3 pixels, small enough to limit the effect of possible contamination from cosmic rays or nearby stars; after inspecting the images, we found no evidence of such contaminations. We estimate and subtract the background using a sky annulus with radius of 30 to 50 pixels. For the UVIS full-frame binned images, we adopt the equivalent: an aperture radius of 1.5 pixels and a sky annulus of 15 to 25 pixels for the background. The Cepheid magnitude  $m_\lambda$  is derived as follows:

$$m_\lambda = m_\lambda^0 + (zp - 25) - \text{ap}_{\text{corr}} \quad (1)$$

where  $m_\lambda^0$  is the measured magnitude,  $zp$  is the magnitude of a star which produces a total count rate of  $1 \text{ e}^- \text{ s}^{-1}$ , and  $\text{ap}_{\text{corr}}$  is the aperture correction from a 3 pixel radius to infinity. We adopted the zero-points from R19 and provided by STScI for each UVIS CCD and each filter (Vega system): 24.711 mag in *F160W*, 25.741 mag and 24.603 mag in *F555W* and *F814W* respectively in chip 1, and 25.727 mag and 24.581 mag in *F555W* and *F814W* respectively in chip 2. We followed R19 and adopted aperture corrections of 0.200, 0.183 and 0.272 mag in *F160W*, *F555W* and *F814W*. To accommodate the potential impact of the gyro drift in the photometry, we adopt a larger aperture of 5 pixels (instead of 3 pixels) for the images that are the most affected by the drift. We measured the ‘‘instant’’ drift for each image by comparing the changes in position for the Cepheid between successive exposures and we found 13 Cepheids with a drift larger than 0.10'' during an ex-

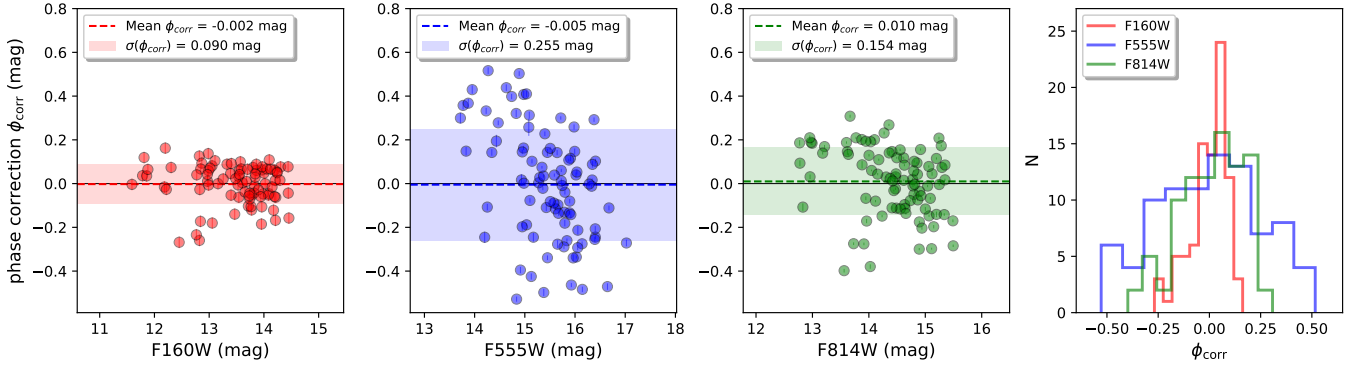


**Figure 4.** Phase corrections derived as the difference between the random epoch magnitude and the intensity averaged mean magnitude in three filters.

**Table 2.** Mean magnitudes of our sample of SMC Cepheids.

Cepheid	R.A.	Dec.	Geo <sup>(a)</sup>	log $P$	$F555W$	$\sigma$	$F814W$	$\sigma$	$F160W$ <sup>(b)</sup>	$\sigma$	$m_H^W$ <sup>(c)</sup>	$\sigma$
	(deg)	(deg)	(mag)	(d)	(mag)		(mag)		(mag)		(mag)	
OGLE-0518	10.801423	-73.325446	-0.089	1.198	15.385	0.017	14.224	0.008	13.161	0.027	12.653	0.028
OGLE-0524	10.828177	-73.338793	-0.089	1.022	15.491	0.012	14.520	0.010	13.693	0.028	13.259	0.028
OGLE-0541	10.873654	-73.002488	-0.052	1.137	15.149	0.018	14.077	0.011	13.088	0.027	12.651	0.028
OGLE-0570	10.947143	-73.240723	-0.075	1.037	15.425	0.011	14.435	0.008	13.496	0.027	13.068	0.028
OGLE-0576	10.963393	-73.332920	-0.084	1.159	15.244	0.011	14.132	0.008	13.107	0.027	12.623	0.028
OGLE-0668	11.157914	-73.136825	-0.056	0.906	15.318	0.017	14.448	0.009	13.669	0.028	13.307	0.029
OGLE-0672	11.165211	-73.263262	-0.069	0.948	15.627	0.010	14.634	0.009	13.673	0.028	13.250	0.028
OGLE-0694	11.223210	-73.289953	-0.069	0.961	16.196	0.016	15.021	0.012	13.885	0.028	13.391	0.029
OGLE-0705	11.264848	-73.307750	-0.070	1.021	15.624	0.017	14.737	0.012	13.699	0.028	13.316	0.029

**Notes:**

(a) The geometric correction is derived using Eqns. 5 and 6.

(b) Does not include CRNL correction ( $0.0293 \pm 0.0023$  mag or 3.8 dex) between SMC and extragalactic Cepheids.

(c) Includes geometric correction and CRNL correction ( $0.0293 \pm 0.0023$  mag or 3.8 dex) between SMC and extragalactic Cepheids.

(This table is available in its entirety in machine-readable form.)

posure in at least one filter (this threshold corresponds to a drift of 0.8 pixels in NIR and 2.5 pixels in UVIS images). For the 5 pixel aperture, we adopt aperture corrections of 0.154, 0.074 and 0.078 mag in  $F160W$ ,  $F555W$  and  $F814W$  respectively (R19).

In five UVIS images (“iev9a4hpq”, “iev9a4hq”, “iev9c2v3q”, “iev9c2v4q”, “iev9tyd8q”), the Cepheid falls close to  $x=1024$ , where there is a detector defect. Vertical lines at  $x=1023$ ,  $x=1024$  and  $x=1025$  are respectively fainter, brighter and brighter than the median of the background by a significant amount. For these images, we corrected for this effect by subtracting the median value of each line (this changes the Cepheid magnitude by 0.010 mag at most).

For UVIS binned images, the *HST* pipeline does not produce CTE-corrected images (“FLC”); only the standard calibrated images (“FLT”) are available. For these images, we applied a small term of 0.015 mag deter-

mined from unbinned images to account for the absence of CTE correction, however this does not affect the main results since it almost always applies to  $F555W$  and  $F814W$  simultaneously, and therefore cancels out in the  $m_H^W$  Wesenheit index (Eq. 2, see §4). We note that this correction might slightly affect the optical Wesenheit (see Eq. 3) but the impact in the P–L relation is nearly negligible. Finally, following R19, we correct for the small difference in the WFC3-UVIS photometry between Shutters A and B by applying  $\pm 0.006$  mag in  $F555W$  and  $\pm 0.0035$  mag in  $F814W$  (Sahu et al. 2014), respectively.

### 3.2. Phase corrections

Our random-phase single-epoch *HST* measurements were transformed into intensity-averaged magnitudes using the well covered  $V$  and  $I$  light curves from the

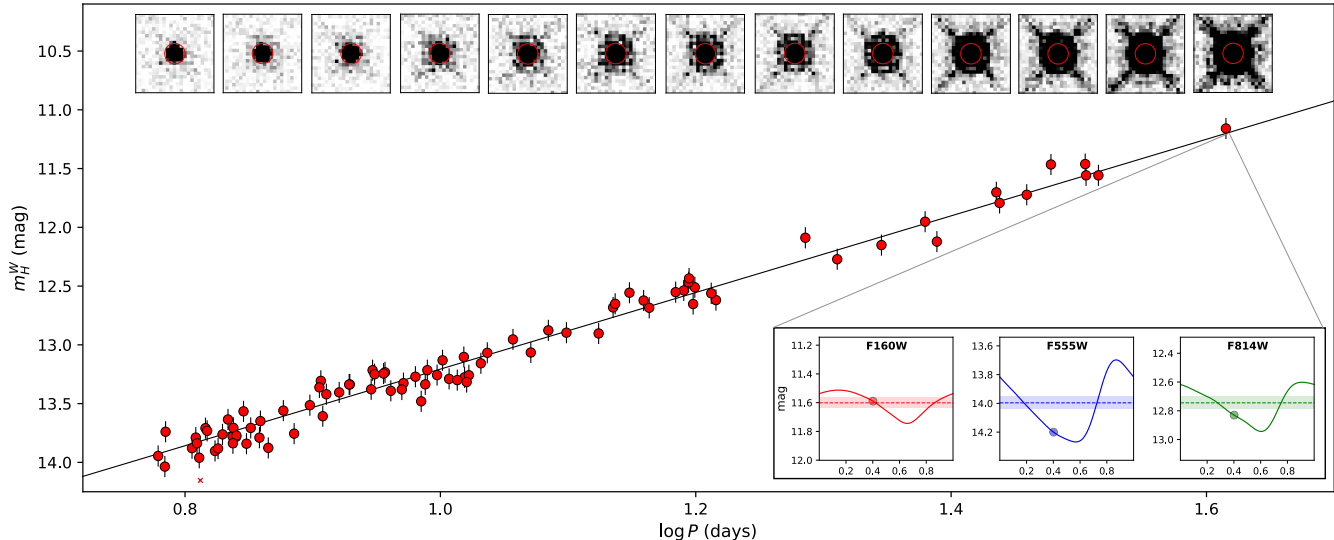


**Figure 5.** P–L relation in the  $m_H^W$  Wesenheit index for our sample of SMC Cepheids. Postage stamps in  $F160W$  are displayed for a number of Cepheids with increasing periods: the stamps are on the same scale with a size of  $1.5''$ , and the red circles are the 3 pixel apertures. An example of light curve fit is shown for the longest-period Cepheid (OGLE-1797) in the three filters.

OGLE-IV survey (Soszyński et al. 2015), obtained with the 1.3-m Warsaw telescope at Las Campanas Observatory in Chile. These light curves were supplemented by additional data points obtained more recently with the same telescope and camera after the release of the OGLE-IV catalog and include the most recent photometric measurements through July 2023 (I. Soszyński, private communication, 2023). These light curves have an average of 59 and 1,118 data points per object in  $V$  and  $I$ , respectively. A few outlier points were rejected from the  $V$ -band light curves for OGLE-1117, 2437 and 0705, and from the  $I$ -band light curves for OGLE-1291, 1477 and 1157. In the case where the  $V$ -band light curve has less than 10 data points (OGLE-2488, 1025, and 1399), we derive it from the  $I$ -band light curve assuming the phase-lag  $\phi_I = \phi_V + 0.023$  and the amplitude ratio  $A_I = 0.6 A_V$ , both derived from our sample of OGLE light curves. We fit the OGLE light curves with Fourier series to create a model from which to estimate the phase corrections and we adapt the number of Fourier modes between 4 and 8 to minimize the  $\chi^2$  of the fit. Finally, for the  $F160W$  filter, we adopted the  $H$ -band templates and phase lag from Inno et al. (2015).

The periods of our Cepheids were taken from OGLE-IV and the phases of our  $HST$  observations are derived from these periods. The phase corrections were derived using the same approach as described in Riess et al. (2018) and are shown in Fig. 4. We find a mean difference of  $-0.002$ ,  $-0.005$  and  $0.010$  mag and standard deviations of  $0.09$ ,  $0.25$  and  $0.15$  mag in  $F160W$ ,  $F555W$

and  $F814W$  respectively. For comparison, R19 found differences of  $-0.001$ ,  $-0.048$  and  $-0.013$  mag with standard deviations of  $0.11$ ,  $0.29$  and  $0.17$  mag in  $F160W$ ,  $F555W$  and  $F814W$  respectively.

## 4. PERIOD-LUMINOSITY RELATIONS

### 4.1. SMC P–L relations

The final intensity averaged magnitudes are listed in Table 2. We combine the three filters to construct the Wesenheit index  $m_H^W$  defined as:

$$m_H^W = F160W - 0.386 (F555W - F814W) \quad (2)$$

where the color coefficient 0.386 is derived from the Fitzpatrick (1999) reddening law assuming  $R_V = 3.3$ , following Riess et al. (2022a). Another secondary quantity used in this work is the optical Wesenheit index, derived under the same assumptions as:

$$m_I^W = F814W - 1.19 (F555W - F814W) \quad (3)$$

We correct for the count rate non-linearity (CRNL) of the WFC3/IR detector, seen as a dimming of fainter sources, which results from photons at low count rates being detected less efficiently than photons at high count rate ( $0.0077 \pm 0.0006$  mag/dex, Riess et al. 2019b): we add  $0.0293 \pm 0.0023$  mag to  $F160W$  measurements, corresponding to a 3.8 dex flux ratio between SMC Cepheids and Cepheids observed in SN Ia host galaxies and NGC 4258. By convention, this is applied to

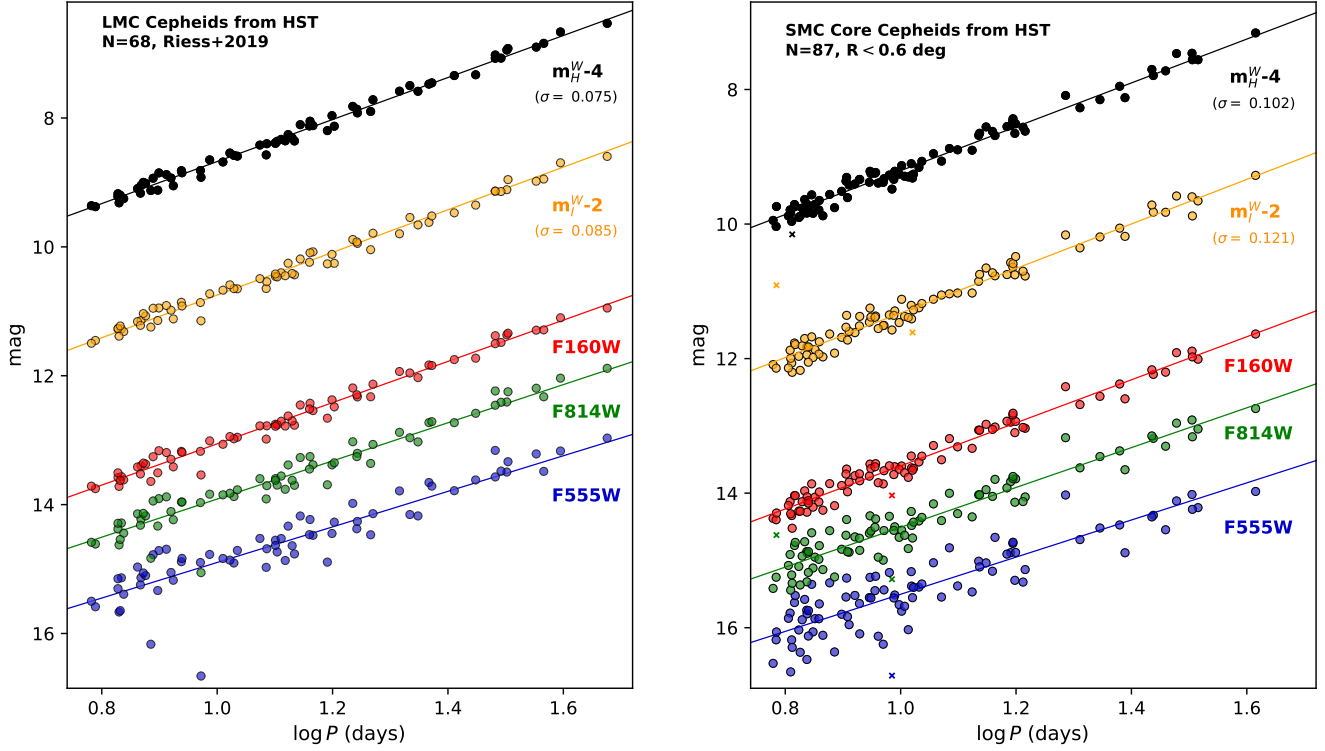


**Figure 6.** Period-Luminosity relations in the 3 *HST* filters and in the  $m_I^W$  and  $m_H^W$  Wesenheit indices. Outliers are shown by small “x” symbols and are excluded from the fit. Left and right panels show the Period-Luminosity relations in the LMC (Riess et al. 2019a) and SMC respectively.

**Table 3.** Cepheid P–L relations from *HST* photometry in the SMC:  $m_H^W = \alpha \log P + \beta$ .

Filter	$\alpha$ (this work)	$\alpha$ (R19)	$\beta$	$\sigma$
<i>F555W</i>	$-2.65 \pm 0.13$	$-2.76 \pm 0.13$	$18.263 \pm 0.031$	0.287
<i>F814W</i>	$-2.98 \pm 0.09$	$-2.96 \pm 0.09$	$17.467 \pm 0.021$	0.195
<i>F160W</i>	$-3.22 \pm 0.06$	$-3.20 \pm 0.04$	$16.795 \pm 0.013$	0.122
$m_I^W$	$-3.37 \pm 0.06$	$-3.31 \pm 0.04$	$16.632 \pm 0.013$	0.121
$m_H^W$	$-3.31 \pm 0.05$	$-3.26 \pm 0.04$	$16.467 \pm 0.011$	0.102

**Notes:** Intercepts in column 4 are derived with slopes fixed to R19 values obtained in the LMC (column 3). All intercepts include geometric corrections and intercepts in *F160W* and  $m_H^W$  include CRNL.

anchor Cepheids rather than those in SN Ia hosts. We also add a small corrective term to account for depth effects in the SMC (see 4th column in Table 2). This geometric correction is discussed in details in §4.2. Finally, we follow R19 and add 0.07 mag in quadrature to the  $m_H^W$  magnitude uncertainties to account for the width of the instability strip.

We adopt a P–L slope of  $-3.26$  mag/dex in  $m_H^W$  from R19 for consistency, and fit the P–L intercept with a

Monte Carlo algorithm. Following R19 we perform a sigma-clipping with a threshold of  $2.75\sigma$  from Chauvenet’s criterion. After rejecting one outlier (OGLE-1455, found at  $3.4\sigma$ ), we obtain a P–L scatter of 0.1017 mag. The dispersion is slightly higher than in the LMC which we attribute to an  $\sim 0.05$  mag dispersion along the line of sight, uncorrected by our simple geometric model, and we combine that in quadrature to the errors for the final errors. The P–L relation is shown in Fig. 5, together with postage-stamp cutout images of Cepheids in *F160W*, as well as an example of light curve fit. Thanks to the higher resolution of *HST*, we avoid crowding and obtain a P–L dispersion that is significantly lower than the ground-based P–L relation derived by the OGLE collaboration in the  $W_{VI}$  index (0.155 mag, Soszyński et al. 2015, thus far the tightest P–L relation in the SMC, see discussion in Appendix B).

The P–L relations obtained in *F160W*, *F555W*, *F814W*,  $m_H^W$  and  $m_I^W$  are shown in Fig. 6, where the slopes are fixed to the R19 values. Table 3 gives the free slopes derived from our sample and the P–L intercepts obtained with the fixed slopes from R19. The  $m_H^W$  free slope is  $-3.31 \pm 0.05$  mag/dex, consistent to within  $1\sigma$  with the  $-3.26$  slope from R19. In the other filters, our slopes are also in excellent agreement with the slopes



from R19. Recent studies have suggested a possible break in the P–L relation (Bhardwaj et al. 2016; Kodric et al. 2018; Bhardwaj 2020): with this low-dispersion data we find no evidence for a break in the P–L relation in the LMC and SMC as presented in Appendix A.

The  $m_H^W$  Wesenheit index defined in Eq. 2 is constructed assuming the Fitzpatrick (1999) reddening law with  $R_V = 3.3$ , which gives a coefficient of  $R = 0.386$ . However Gordon et al. (2003) suggested that the SMC dust corresponds better to  $R_V = 2.74$ , which would give  $R = 0.362$ . Using this alternate definition of  $m_H^W$  yields a slightly larger P–L scatter of 0.1024 mag. Formally, the fact that  $R_V = 2.74$  results in a larger scatter compared to  $R_V = 3.3$ , if at all significant, argues against it providing a better description of the SMC dust. We, therefore, adopt  $R_V = 3.3$  as in our previous work.

#### 4.2. The geometry of the SMC

The SMC is known to have an elongated structure, which can complicate distance measurements based on this dwarf galaxy. From a sample of Cepheids, Mathewson et al. (1988) found a significant line-of-sight depth of about 20 kpc (compared to its distance of  $\sim 62$  kpc) and that the northeastern section of the bar is 10 – 15 kpc closer than the southern section. Nidever et al. (2013) also showed that the optical depth in the eastern part of the SMC is two times higher than in the western part, and that the eastern part comprises of two groups of stars with different mean distances. More recently, Murray et al. (2024) presented evidence that the SMC is actually composed of two substructures with distinct chemical composition separated by  $\sim 5$  kpc along the line of sight. As a result, any study of SMC Cepheids must include their non-negligible spread in distance.

In order to mitigate the impact of its elongated shape, a first solution is to limit the sample to a narrow region in the SMC core. Breuval et al. (2022) showed that the ideal region (based on reducing the P–L scatter) is a radius of 0.6 deg around the SMC center, where the number of Cepheids is still sufficient to populate the P–L relation, while the residual geometry effects are minimized. For example, adopting a Cepheid sample in a region of  $R = 0.6$  deg compared to a larger region of  $R = 2.5$  deg reduces the P–L scatter by 0.02 mag (see Fig. 1) and changes the P–L intercept by 0.050 mag, so that extending to the larger radius results in a significant degradation in accuracy with respect to the uncertainties reported in Tab 3.

Additionally, one can attempt to correct for the differential depths of each Cepheid by adopting a planar model for the SMC. For example, Breuval et al. (2021,

2022) corrected for the SMC depth by adopting the planar model described by DEBs from Graczyk et al. (2020). The corrected distance to each Cepheid is:

$$d(x, y) = +3.086x - 4.248y + d_{\text{SMC}} \quad (4)$$

where  $(x, y)$  are the cartesian coordinates of the Cepheids obtained from their equatorial coordinates  $(\alpha, \delta)$  (see Breuval et al. 2021, §3.3 for the transformations), considering the SMC center at  $(12^\circ.54, -73^\circ.11)$  from Ripepi et al. (2017), and  $d_{\text{SMC}} = 62.44 \pm 0.47 \pm 0.81$  kpc is the mean SMC distance from Graczyk et al. (2020), based on DEBs. The geometric correction we apply to each Cepheid,  $\text{mag}_{\text{corr}}$ , is derived with:

$$\text{mag}_{\text{corr}} = 5 \log_{10}(d_{\text{SMC}}/d(x, y)) \quad (5)$$

This correction is valid as long as Cepheids and DEBs share the same center and have a similar spatial distribution, which is true near the SMC center but may not be the case in the outskirts. Also, the SMC geometry is not planar at large scales, but this is a good approximation for the core region. Using this correction we obtain a P–L scatter of 0.1022 mag. We then refined this geometry model based on our own sample of Cepheids: we varied both coefficients and retained the solution that minimizes the  $\chi^2$  of the P–L relation. We find an optimal geometry of:

$$d(x, y) = +3.480x - 2.955y + d_{\text{SMC}} \quad (6)$$

which gives a final P–L scatter of 0.1017 mag. We note that the uncertainties of the geometric coefficients are of the order of  $\pm 1$ . These corrections have a mean value of  $-0.003$  mag and a dispersion of 0.047 mag, with a minimum and maximum of  $-0.088$  mag and  $+0.098$  mag. Our SMC geometry is in good agreement with the distribution of SMC DEBs from Graczyk et al. (2020), with the geometry of SMC Cepheids from Scowcroft et al. (2016) obtained from *Spitzer* mid-infrared observations of 90 Cepheids, and also with the VMC survey by Ripepi et al. (2017) with NIR light curves of 717 SMC Cepheids, and with Jacyszyn-Dobrzniecka et al. (2016) and their geometry model derived from optical light curves of 2646 fundamental mode Cepheids from the OGLE survey.

In this section, we showed how the considerable line-of-sight depth of the SMC might affect the P–L relation and how we can greatly mitigate its impact for distance measurements. The SMC geometry is still challenging and its structure must be better understood (Murray et al. 2024), but for our purposes, the present Cepheid-based geometric corrections and core-region sample best reduce their impact, and any residual effects only slightly increase the P–L scatter.

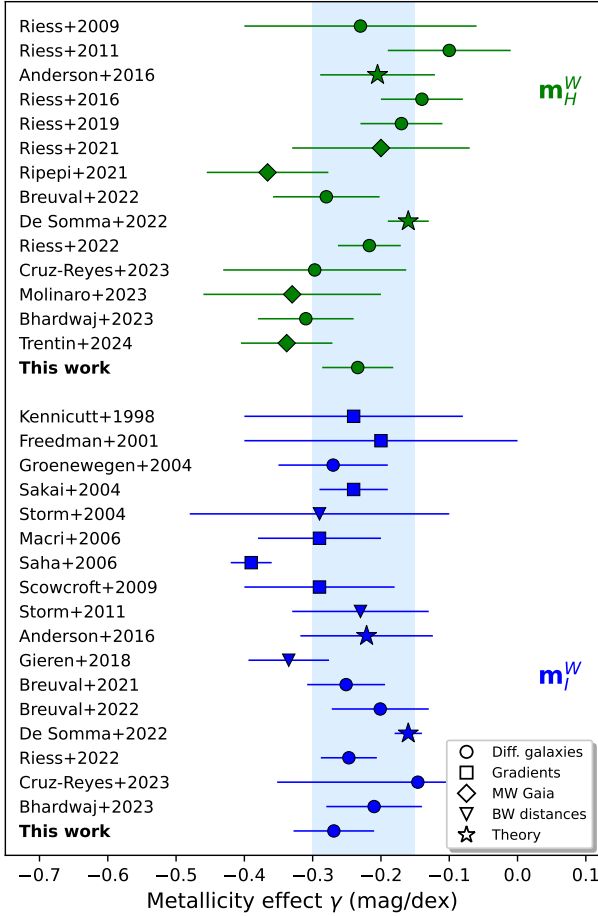


**Figure 7.** Metallicity dependence in  $m_H^W$  and  $m_I^W$  from the literature. Some issues were identified in the results by Wielgórski et al. (2017), Freedman & Madore (2011) and Madore & Freedman (2024), therefore they are not shown in this figure (see discussion in Breuval et al. 2022, §5.5). The blue region covers  $-0.15$  to  $-0.30$  mag/dex, where most values are found.

#### 4.3. Calibration of the metallicity effect in the HST/WFC3 photometric system

The Cepheid metallicity effect has been a source of intense study for over three decades (Freedman & Madore 1990; Freedman et al. 2001; Sakai et al. 2004). In previous generation measurements of the Hubble constant, which relied on comparisons between Cepheids in the low-metallicity LMC and metal-rich spirals, this term played a significant role. More recent determinations of  $H_0$  make use of metal-rich calibrations in NGC 4258 and from improved Milky Way parallaxes, thus reducing the full impact of this term to  $< 1$  km/s/Mpc.

In the regime covered by SNe Ia host galaxies (with metallicities between Milky Way and LMC Cepheids), there is a consensus for its sign and value ( $\gamma \sim$

$-0.25$  mag/dex) thanks to improved distances and metallicities (Breuval et al. 2022; Romaniello et al. 2022; Trentin et al. 2024, see Figure 7 for a literature summary). However, this term is still relatively weakly constrained in the metal-poor regime ( $[\text{Fe}/\text{H}] < -0.5$  dex). Its calibration over a larger metallicity range requires combining precise abundance measurements in multiple galaxies with homogeneous Cepheid photometry in a consistent system. Our sample of SMC Cepheids with HST/WFC3 photometry represents a unique opportunity to extend the calibration of this effect over a metallicity range twice as large as that currently available.

We compile three samples all with identical-system photometry:

- 67 Milky Way Cepheids from Riess et al. (2021) with precise *Gaia* DR3 parallaxes including the Lindegren et al. (2021) zero-point and the residual  $14 \mu\text{as}$  correction determined from Cepheids,
- 70 LMC Cepheids from R19,
- 87 SMC Cepheids from the present paper.

Metallicities of Milky Way Cepheids are taken from Bhardwaj et al. (2023) and were measured recently using high-resolution spectra obtained with ESPaDOnS on CFHT. The mean metallicity of the Milky Way sample is  $+0.033 \pm 0.013$  dex and the dispersion is 0.11 dex. For LMC Cepheids, we adopt the metallicities from Romaniello et al. (2022) obtained with UVES on the ESO VLT, with individual measurements for all Cepheids and a mean value of  $[\text{Fe}/\text{H}] = -0.409 \pm 0.003$  dex, and a dispersion of 0.076 dex. Finally, we adopt the new metallicity measurements of SMC Cepheids from Romaniello et al. (2024, in prep.) which include 44 Cepheids of our sample, a mean value of  $[\text{Fe}/\text{H}] = -0.785 \pm 0.012$  dex, and a dispersion of 0.082 dex.

To measure the metallicity effect, we first fit the P–L intercept  $\beta$  in each galaxy with a fixed slope of  $-3.26$  mag/dex. Then, we fit a linear relation between the intercept and the mean metallicity (see method in Breuval et al. 2022):  $\beta = \gamma [\text{Fe}/\text{H}] + \delta$ . In the three galaxies, we conservatively assume an uncertainty of 0.05 dex for the mean metallicity and we add the distance uncertainties in quadrature to the intercept errors. We obtain  $\gamma = -0.234 \pm 0.052$  mag/dex, where the uncertainties are estimated via a Monte Carlo algorithm (Fig. 8). In the optical ( $m_I^W$ ), we find  $\gamma = -0.264 \pm 0.058$  mag/dex.

These values are very consistent with other recent measurements based on a combination of geometric distances in the Milky Way and Magellanic Cloud Cepheids (Breuval et al. 2021, 2022; Bhardwaj et al. 2023; Cruz

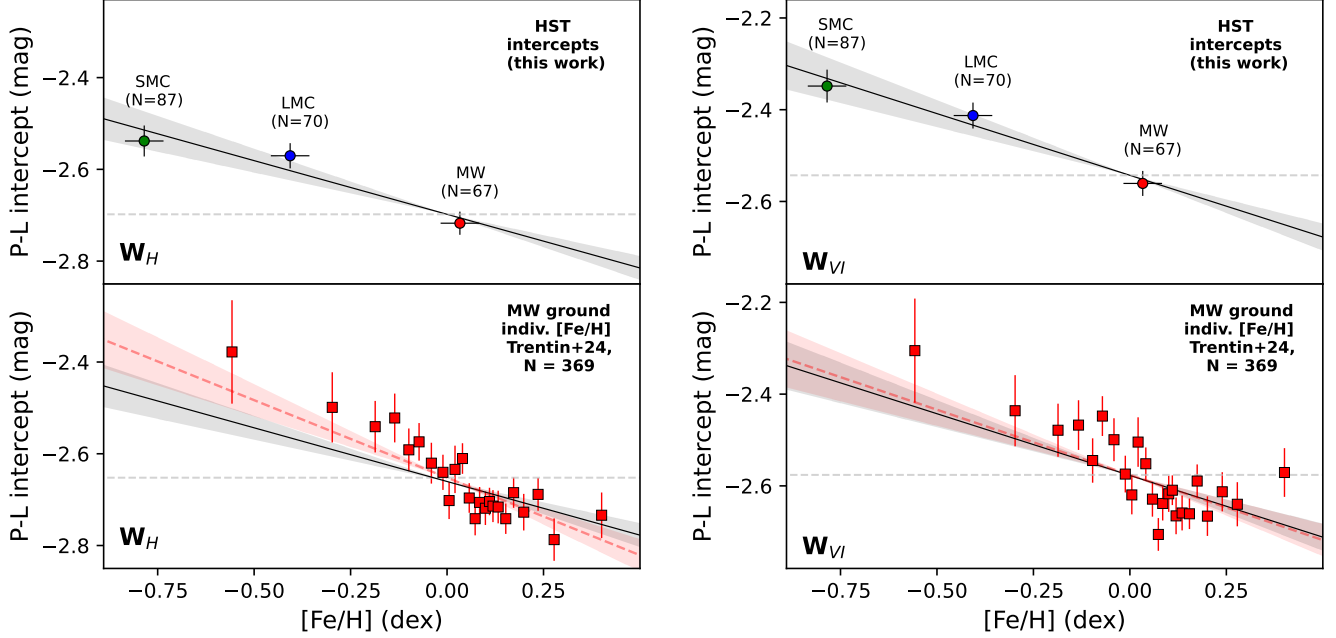


**Figure 8.** (Top): P–L intercept (at  $\log P = 0$ ) in the Milky Way (red), LMC (blue) and SMC (green) based on *HST* photometry versus  $[\text{Fe}/\text{H}]$ , where the slope is the metallicity dependence  $\gamma$ . (Bottom): Binned data (a square symbol is the average of 15 data points) from Trentin et al. (2024) based on ground-based photometry, *Gaia* DR3 parallaxes and high resolution spectroscopic measurements in the Milky Way. The solid black line is the slope obtained in the present paper,  $\gamma(W_H) = -0.234$  mag/dex and  $\gamma(W_{VI}) = -0.264$  mag/dex, and the dashed red line is the slope from Trentin et al. (2024). The left and right panels show the  $m_H^W$  and  $m_I^W$  Wesenheit indices respectively (their absolute magnitudes are called  $W_H$  and  $W_{VI}$ ).

Reyes & Anderson 2023). Independent calibrations of the metallicity effect based exclusively on several hundred Milky Way Cepheids with *Gaia* DR3 parallaxes from the C-MetaLL project including new spectra of very metal poor Cepheids have resulted in stronger effects of the order of  $-0.4$  mag/dex in the *Gaia*  $W_G$ , optical  $W_{VI}$  and NIR  $W_{VK}$ ,  $W_{JK}$  Wesenheit indices (Ripepi et al. 2022; Trentin et al. 2024; Bhardwaj et al. 2024). However, they recover the canonical result of  $\sim -0.25$  to  $-0.3$  dex in the specific  $W_H$  Wesenheit index used in the SH0ES distance ladder and good agreement with the LMC DEB distance (see Trentin et al. 2024, Figure 16).

An outlier to this consensus comes from one study by Madore & Freedman (2024), which selects Cepheid calibrations from TRGB distances rather than the geometric anchors, comparing 28 hosts and concluding that  $\gamma \sim 0$  for  $m_I^W$ . However, measuring the Cepheid metallicity effect by comparing Cepheid and TRGB distances requires that TRGB distances be independent of metallicity, which is not certain (see for example Wu et al. 2023). More importantly, the Cepheid data for this study relies heavily on older and relatively inhomogeneous data sources (21 different photometric systems) and smaller samples which have been superseded in

recent studies. Compared to the combination of *HST* measurements of Cepheids in the SMC, LMC and Milky Way (which produced  $\gamma = -0.264 \pm 0.058$  mag/dex for  $m_I^W$  here), Madore & Freedman (2024) excludes all Milky Way Cepheids (and *Gaia* parallaxes) and finds at face value  $\gamma = -0.096$  mag/dex between the SMC and LMC, only half the size of our result. However, their SMC sample is based on only 9 fundamental-mode Cepheids, while the OGLE survey provides more than 2,300 Cepheids in the SMC (Soszyński et al. 2015, or the 88 here identically calibrated to those in the LMC and MW). Some of the evidence for their low absolute value of  $\gamma$  is based on the four hosts with the lowest metallicity, namely Sextans A and B, WLM and IC 1613; for these, the Cepheid metallicity estimate of  $\sim -1.3$  dex is based on the host metallicity (Sakai et al. 2004). Such a low metallicity value would be surprising for any Population I Cepheid, with no such spectroscopic examples known in the MW Trentin et al. (2024). Indeed, spectra of young massive stars in WLM ( $-0.5$  to  $-1.0$  dex with a mean of  $-0.87$  dex, Urbaneja et al. 2008) are more metal rich than that value of  $-1.3$  dex used for that host. If the metallicities of new massive stars like Cepheids in these metal poor hosts are greater than the host mean, this would lead to an underestimate of the metallicity term.

**Table 4.** Uncertainty in  $H_0$  from leading term, geometric calibration of Cepheids (%).

Term	Description	Riess et al. (2022a,b)			This paper			
		LMC	MW	N4258	LMC	MW	N4258	SMC
$\sigma_{\mu, \text{anchor}}$	Anchor distance	1.2	0.8 <sup>(a)</sup>	1.5 <sup>(b)</sup>	1.2	0.8 <sup>(a)</sup>	1.5 <sup>(b)</sup>	1.5
$\sigma_{\text{PL}, \text{anchor}}$	Mean of P–L in anchor	0.4	...	1.0	0.4	...	1.0	0.5
$R\sigma_{\lambda, 1, 2}$	Zeropoints, anchor-to-host	0.1	0.1 <sup>(a)</sup>	0.0	0.1	0.1 <sup>(a)</sup>	0.0	0.1
$\sigma_Z$	Cepheid metallicity, anchor-hosts	0.4	0.15	0.15	0.4	0.1	0.1	0.5
	Subtotal per anchor	1.4	0.8	1.8	1.4	0.8	1.8	1.7
First Rung Total		0.65			0.60			

NOTE— (a) Includes both field Cepheids and cluster Cepheids; (b) Reid et al. (2019).

Obtaining spectra of Cepheids in these hosts would be warranted to resolve the issue. Our calibration of the metallicity effect, based on direct measurements for a large number of Cepheids, is in excellent agreement with previous distance-ladder studies by the SH0ES team and other independent works. (Fig. 7).

## 5. THE HUBBLE CONSTANT

Since Riess et al. (2022a), there have been several updates that could lead to an improved local measurement of  $H_0$ . These include the cluster Cepheids from Riess et al. (2022b), the pairwise SNe Ia covariance analysis based on spectral similarities from Murakami et al. (2023), and the revised metallicity measurements from Bhardwaj et al. (2023). With the results presented here, we are now able to include the SMC as a bona-fide fourth anchor of the distance ladder, in addition to (1) *Gaia* DR3 parallaxes of Milky Way Cepheids (Riess et al. 2021), (2) late-type DEBs in the LMC (Pietrzyński et al. 2019; Riess et al. 2019a), and (3) the water-maser host galaxy NGC 4258 (Reid et al. 2019). The SMC satisfies the two criteria established in Riess et al. (2022a) for the other 3 anchors: a geometric distance determination and Cepheid photometry measured on a homogeneous *HST* photometric system. We combine the 88 core SMC Cepheids measured here, the DEB distance from Graczyk et al. (2020), and SMC Cepheid metallicity measurements from Romaniello et al. (2024, in prep.) using the same formalism presented in Riess et al. (2022a). We find  $H_0 = 73.17 \pm 0.86 \text{ km s}^{-1} \text{ Mpc}^{-1}$ , a 1.2% determination of the Hubble constant including systematic uncertainties. As shown in Table 4, including the SMC reduces the error in the first rung from 0.65% to 0.60%. This reduction is slightly less than what would occur if all anchors had equal weight; however, the combined constraints from *Gaia* MW field and cluster-hosted Cepheids have nearly double the preci-

sion of the SMC. Somewhat greater leverage comes from the inclusion of the SMC in the global determination of the metallicity term due to its low metallicity. With the SMC, the global fit of the distance ladder yields a metallicity dependence of  $\gamma(m_H^W) = -0.19 \pm 0.047 \text{ mag/dex}$ . This represents a 40% improvement over the uncertainty of  $\pm 0.067 \text{ mag/dex}$  obtained without the SMC<sup>1</sup>. Unlike in §4.3, here we use a covariance matrix to take into account that the LMC and SMC geometric distances have a common systematic error (their relative distance is measured better than their individual distances), which helps constrain the difference in Cepheid brightness. We note that the global metallicity scale used in the SH0ES distance ladder is based on [O/H], rather than [Fe/H] as used in the previous section. This is most relevant when including low metallicity hosts like the SMC, with their enhanced  $\alpha/\text{Fe}$  abundances; [O/Fe] is  $\sim 0.2$  for the SMC Cepheids (Romaniello et al. 2024, in prep.), higher than the value of  $\sim 0.06$  seen at higher metallicities such as in the MW (e.g. Luck & Lambert 2011). This somewhat compresses the [O/H] scale versus [Fe/H], leading to a smaller (in absolute value) metallicity term than from the earlier sections. With the SMC as the only anchor for the distance ladder, we obtain  $H_0 = 74.1 \pm 2.1 \text{ km s}^{-1} \text{ Mpc}^{-1}$ , which shows the good consistency of the SMC with the other three anchors.

## 6. DISCUSSION

We presented the first photometric measurements of SMC Cepheids with the *Hubble* Space Telescope Wide Field Camera 3, using the same photometric system as the rest of the SH0ES distance scale. Combining the

<sup>1</sup> We note for completeness that the lower metallicity uncertainty was already included in R22 thanks to the combined use of SMC and LMC ground-based data on the same photometric system, but without the value of the Cepheid geometric calibration.

**Table 5.** SMC Period-Luminosity relations from the literature.

Filter	Def.	Reference	Slope (mag/dex)	Intercept (mag)	$\sigma$ (mag)	$N$	$R_{\max}$ (deg)	Telescope	
$V$		Soszyński et al. (2015)	$-2.898 \pm 0.018$	$17.984 \pm 0.008$	0.266	4747	3 (98%)	Warsaw telescope,	
$I$		Soszyński et al. (2015)	$-3.115 \pm 0.015$	$17.401 \pm 0.007$	0.215	4940	6 (100%)	Las Campanas	ground
$m_{1,\text{grd}}^W$	(a)	Soszyński et al. (2015)	$-3.460 \pm 0.011$	$16.493 \pm 0.005$	0.155	4743		Observatory	
$G$		Ripepi et al. (2023)	$-2.830 \pm 0.033$	$17.757 \pm 0.026$	0.251	843	3 (99%)	<i>Gaia</i>	space
$m_G^W$	(b)	Ripepi et al. (2023)	$-3.382 \pm 0.021$	$16.592 \pm 0.017$	0.156	839	5 (100%)		
$J$		Ripepi et al. (2017)	$-3.070 \pm 0.026$	$16.778 \pm 0.021$	0.196	821			
$K_S$		Ripepi et al. (2017)	$-3.224 \pm 0.023$	$16.530 \pm 0.018$	0.167	821	3 (98%)	ESO/VISTA	ground
$m_{JK}^W$	(c)	Ripepi et al. (2017)	$-3.334 \pm 0.021$	$16.363 \pm 0.017$	0.158	821	6.5 (100%)	telescope	
$m_{VK}^W$	(d)	Ripepi et al. (2017)	$-3.291 \pm 0.021$	$16.375 \pm 0.017$	0.155	821			
[3.6 $\mu\text{m}$ ]		Scowcroft et al. (2016)	$-3.306 \pm 0.050$	$16.492 \pm 0.017$	0.161	90	3 (98%)	<i>Spitzer</i>	space
[4.5 $\mu\text{m}$ ]		Scowcroft et al. (2016)	$-3.207 \pm 0.060$	$16.357 \pm 0.018$	0.164	90	6.5 (100%)		
$m_I^W$	(e)	<b>This work</b>	$-3.31 \pm 0.04$	$16.632 \pm 0.013$	<b>0.121</b>	87	0.6	<i>Hubble</i>	space
$m_H^W$	(f)	<b>This work</b>	$-3.26 \pm 0.04$	$16.467 \pm 0.011$	<b>0.102</b>	87	0.6		

(a):  $m_{1,\text{grd}}^W = I - 1.55(V - I)$ , (b):  $m_G^W = G - 1.90(BP - RP)$ , (c):  $m_{JK}^W = K - 0.69(J - K)$ , (d):  $m_{VK}^W = K - 0.13(V - K)$ ,  
(e):  $m_I^W = F814W - 1.19(F555W - F814W)$ , (f):  $m_H^W = F160W - 0.386(F555W - F814W)$ .

high resolution of *HST* with a sample of 88 Cepheids in the core of the SMC, we mitigate the impact of crowding and of the SMC line-of-sight depth, and obtain the lowest dispersion for the Cepheid P–L relation in this galaxy to date:  $\sigma = 0.102$  mag (a comparison between *HST* and ground-based photometry is presented in Appendix B). Some recent P–L relations from the literature obtained in different photometric systems and filters are listed in Table 5. Thanks to the low metallicity of SMC Cepheids, we calibrate the metallicity dependence of Cepheids on a range twice larger than previous studies and we find excellent agreement with the literature with  $\gamma = -0.234 \pm 0.052$  mag/dex. Although it would not directly impact the  $H_0$  value, this dependence needs to be better calibrated in the most metal-poor regime beyond  $[\text{Fe}/\text{H}] < -0.7$  dex, for example in Local Group galaxies WLM, IC1613, Sextans A and B using spectra of Cepheids there, and where possible non-linearities could be investigated.

In this work, we provide a new calibrating galaxy for the first rung of the distance scale with the first *HST* photometric measurements of SMC Cepheids, increasing the number of geometric anchors from three to four, which yields a 1.2% measurement of the Hubble constant,  $H_0 = 73.20 \pm 0.86$  km s $^{-1}$  Mpc $^{-1}$ . The small number of geometric anchors is primarily due to limitations in the late-type DEBs method. Eclipsing binaries are rare systems in which two stars orbit each other, and their orbital plane is aligned in such a way that each star regularly passes in front of the other, causing an eclipse. They present regular light curves with well-defined eclipses. “Detached” systems are well-separated

and do not transfer mass between the components. The distance to these systems can be derived by comparing the components’ linear diameter, obtained from the analysis of the photometric and radial velocity curves (Guinan et al. 1998; Fitzpatrick et al. 2003), and their angular diameter, measured using surface brightness-color relations. While late-type DEBs provide unprecedented precision for the geometric distances to the LMC and SMC, the downside of this method is that these systems are faint, typically  $m_V \sim 18$  mag at the distance of the SMC, which makes them difficult to observe in more distant galaxies. On the other hand, early-type DEBs are much brighter and can reach  $\sim 1$  Mpc, including nearby galaxies M31 and M33 (Bonanos et al. 2006). The method to measure early-type DEB distances is different from the late-types as it relies on model atmosphere theory, instead of the 1% precision surface brightness color relation used for late-type DEBs in the LMC and calibrated empirically (Pietrzyński et al. 2019). This relation is not yet calibrated on the color range applicable to early-type DEBs ( $-1 < V - K < 0$ ). New results are expected from ongoing interferometric measurements of angular diameters for these stars in the solar neighborhood and in the LMC (Challouf et al. 2014; Taormina et al. 2020). This work is extremely important, as future geometric distances to M31 and M33 will directly provide two additional anchors for the distance scale, where Cepheid photometry is already available in the HST/WFC3 photometric system (Li et al. 2021; Breuval et al. 2023).

Although the LMC geometric distance from Pietrzyński et al. (2019) remains the best DEB-based

calibrator for the first rung of the distance ladder, the low metallicity and the large number of Cepheids in its core region make the SMC a powerful addition to the set. The SMC also has a historical importance as it is the galaxy where the P–L relation was first discovered and established by Henrietta Leavitt (Leavitt & Pickering 1912). Our consistent photometric measurements of Cepheids in the core of the SMC fall well within the distance ladder established from the 3 other anchor galaxies. With the addition of the SMC as a fourth anchor, the late universe measurement of the Hubble constant from the distance ladder moves closer to the goal of 1% accuracy.

### ACKNOWLEDGEMENTS

We are grateful to the OGLE team for providing us with the most recent light curves for our sample of SMC Cepheids. Support for this work was provided by the National Aeronautics and Space Administration

(NASA) through program No. GO-17097 from the Space Telescope Science Institute (STScI), which is operated by AURA, Inc., under NASA contract No. NAS 5-26555. This research is based primarily on observations with the NASA/ESA *Hubble* Space Telescope, obtained at STScI, which is operated by AURA, Inc., under NASA contract No. NAS 5-26555. This research was funded in part by the National Science Centre, Poland, grant no. 2022/45/B/ST9/00243. This research was supported by the Munich Institute for Astro-, Particle and BioPhysics (MIAPbP), which is funded by the Deutsche Forschungsgemeinschaft (DFG, German Research Foundation) under Germany’s Excellence Strategy – EXC-2094 – 390783311. L.B. would like to thank Boris Trahin, Laura Herold, Siyang Li and Javier H. Minniti for helpful discussions. The data presented in this paper were obtained from the Mikulski Archive for Space Telescopes (MAST) at the Space Telescope Science Institute. The specific observations analyzed can be accessed via [doi:10.17909/08t1-3x45](https://doi.org/10.17909/08t1-3x45).

### APPENDIX

#### A. A BREAK IN THE CEPHEID P–L RELATION?

Here we investigate the presence of a possible discontinuity in the P–L slope (see Bhardwaj et al. 2016). In the present SMC sample and in the LMC sample from R19, we separate Cepheids into two subsamples, short vs long period Cepheids. For different values of the pivot period comprised between  $\log P = 0.85$  and  $\log P = 1.5$  (which leaves at least 10% of the initial sample on each side of the pivot period), we fit the P–L slope with a Monte Carlo algorithm taking into account the error bars and we compare the P–L slope in both regimes. Fig. 9 shows the difference between the long- and short-period slopes divided by their errors in quadrature at different pivot periods. The LMC and SMC samples are represented in blue and green, and show a maximum slope difference of  $1.8\sigma$  and  $2.4\sigma$  respectively.

However, we must account for the random chance of finding a break at any  $\log P$ . In order to estimate the likelihood of a break in the P–L relation, we create 10,000 random fake Cepheid samples ( $N=88$ ) with the same P–L scatter as in the SMC ( $\sigma = 0.102$  mag). For each fake sample, we fit the P–L slope at short and long periods for a break located at different  $\log P$  values. For these different  $\log P$  breaks, we record the highest slope difference and we find that 51% of the time, the slopes at short vs long periods disagree to higher than 2.4 times the combined error (i.e. higher than the value we found in the SMC). Fig. 9 also shows the 99% and 95% confidence limits of this test. We conclude that it is not surprising to measure a change in the P–L slope which is 2.4 times the error as we find in the SMC because there is so much freedom in the search for a break. Regarding the position of the break, there is no preferred value but it occurs slightly more often at short ( $\log P \sim 0.95$ ) and long ( $\log P \sim 1.45$ ) periods, also where the samples are more limited. In conclusion, we find no evidence of a break in the P–L relation for our sample of LMC or SMC Cepheids.

#### B. COMPARISON BETWEEN *HST* AND GROUND-BASED PHOTOMETRY

In order to highlight the significant improvements of *HST* photometry over past ground-based measurements, we simulated a ground-based seeing of  $0.2''$  to  $1.4''$  by binning *F160W* *HST* images. The left panel of Fig. 10 shows the P–L scatter with different binning levels: the scatter reaches 0.15 mag with a  $1''$  seeing and a scatter as high as 0.20 mag for a seeing of  $1.4''$ . The NIR P–L relation obtained by Ripepi et al. (2017) with the VLT/VISTA telescope and a seeing of  $0.9''$  (Cioni et al. 2011) has a scatter of 0.16 mag, close to the result of our simulation, but slightly higher due to additional geometry (depth) effects. The right panel of Fig. 10 shows that a common seeing of

1.2'' can also bias the P–L intercept by up to 0.20 mag, therefore affecting the distances derived from these calibrations.

C. THE SMC STRUCTURE ON SMALLER SCALES

Fig. 11 shows the effect of including progressively smaller regions in the LMC and SMC samples; although there is an apparent decrease in the dispersion in the SMC P–L relation for radii smaller than 0.12 deg, the effect is modest and of limited statistical significance. We note that if the geometry of the SMC is akin to a bar, depth effects on scales comparable to the bar’s minor axis will remain even for very small regions near the center.

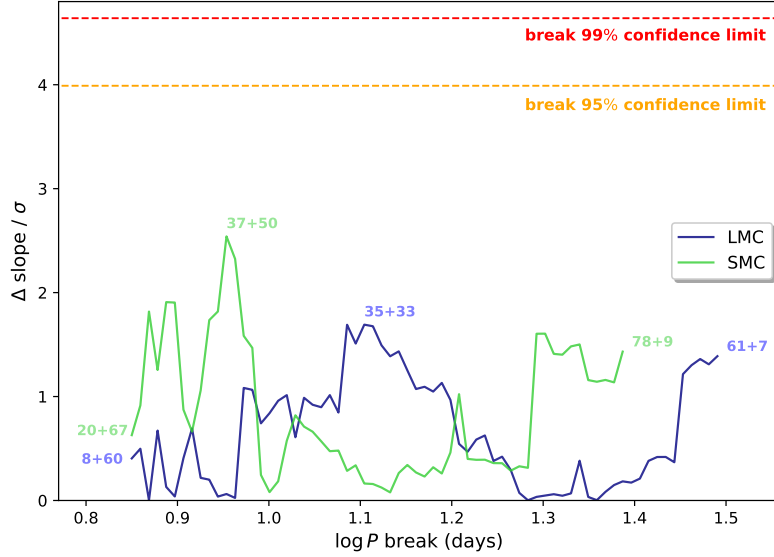


**Figure 9.** Slope difference between the long and short period regime divided by their errors in quadrature, for different values of the pivot period. The numbers  $N + M$  give the number of Cepheids in the short ( $N$ ) and long ( $M$ ) period subsamples.

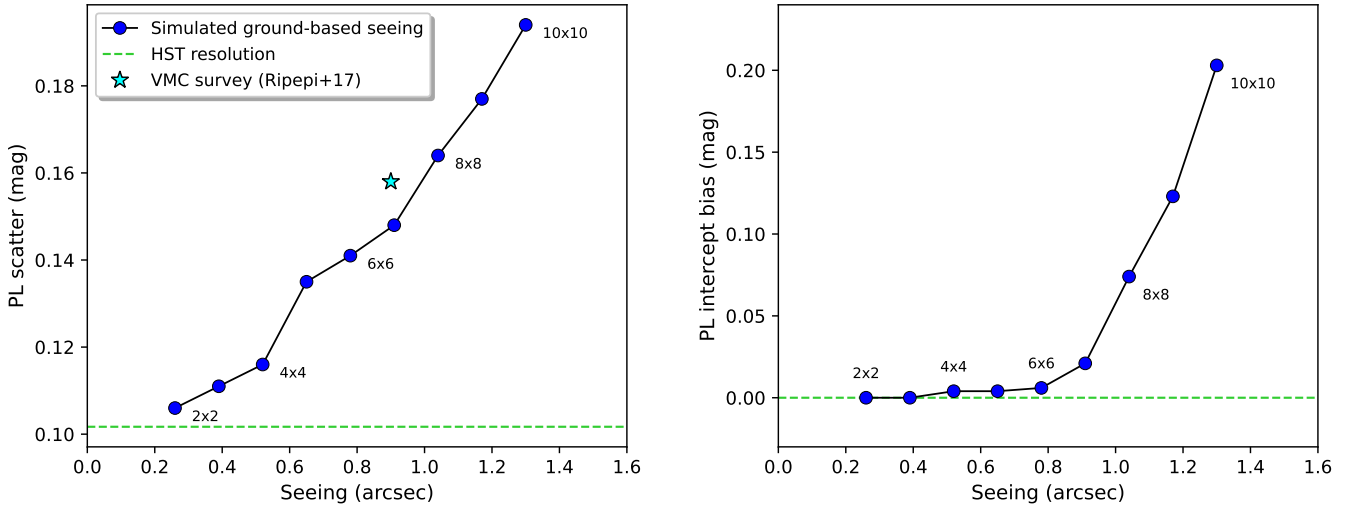


**Figure 10.** By binning *HST* *F160W* images, we simulate a ground-based seeing and we recover the P–L scatter (left) and the bias on the P–L intercept (right). The blue star shows the P–L scatter from Ripepi et al. (2017) obtained with the VISTA telescope with a seeing of 0.9''.

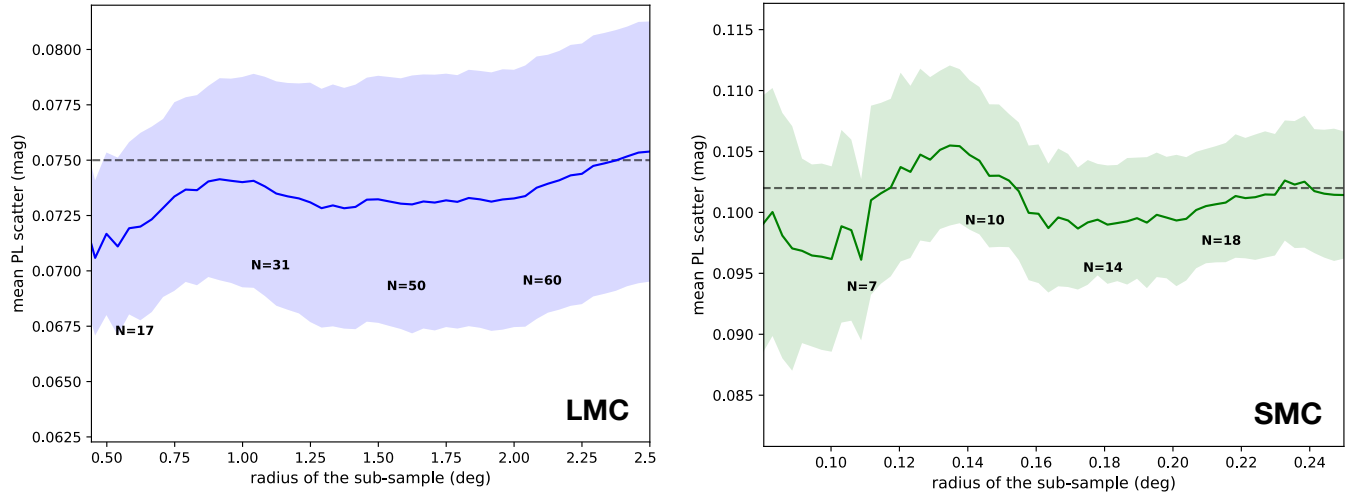


**Figure 11.** Mean P–L scatter for Cepheid subsamples in different region sizes, in the LMC sample from R19 (left) and our SMC sample (right). The mean number of Cepheids are shown in black for a few subsamples. The horizontal dashed line shows the scatter of the full Cepheid sample (in the LMC:  $N = 68$ ,  $\sigma = 0.075$  mag, in the SMC:  $N = 87$ ,  $\sigma = 0.102$  mag).

## REFERENCES

- Bhardwaj, A. 2020, *Journal of Astrophysics and Astronomy*, 41, 23
- Bhardwaj, A., Kanbur, S. M., Macri, L. M., et al. 2016, *MNRAS*, 457, 1644
- Bhardwaj, A., Riess, A. G., Catanzaro, G., et al. 2023, *ApJL*, 955, L13
- Bhardwaj, A., Ripepi, V., Testa, V., et al. 2024, arXiv e-prints, arXiv:2401.03584
- Bonanos, A. Z., Stanek, K. Z., Kudritzki, R. P., et al. 2006, *ApJ*, 652, 313
- Breuval, L., Riess, A. G., Kervella, P., Anderson, R. I., & Romaniello, M. 2022, *ApJ*, 939, 89
- Breuval, L., Kervella, P., Wielgórski, P., et al. 2021, *ApJ*, 913, 38
- Breuval, L., Riess, A. G., Macri, L. M., et al. 2023, *ApJ*, 951, 118
- Challouf, M., Nardetto, N., Mourard, D., et al. 2014, *A&A*, 570, A104
- Cioni, M. R. L., Clementini, G., Girardi, L., et al. 2011, *A&A*, 527, A116
- Cruz Reyes, M., & Anderson, R. I. 2023, *A&A*, 672, A85
- Di Valentino, E., Mena, O., Pan, S., et al. 2021, *Classical and Quantum Gravity*, 38, 153001
- Eddington, A. S. 1917, *The Observatory*, 40, 290
- Fitzpatrick, E. L. 1999, *PASP*, 111, 63
- Fitzpatrick, E. L., Ribas, I., Guinan, E. F., Maloney, F. P., & Claret, A. 2003, *ApJ*, 587, 685
- Freedman, W. L., & Madore, B. F. 1990, *ApJ*, 365, 186
- . 2011, *ApJ*, 734, 46
- Freedman, W. L., Madore, B. F., Gibson, B. K., et al. 2001, *ApJ*, 553, 47
- Gaia Collaboration, Brown, A. G. A., Vallenari, A., et al. 2021, *A&A*, 649, A1
- Gieren, W., Storm, J., Konorski, P., et al. 2018, *A&A*, 620, A99
- Gordon, K. D., Clayton, G. C., Misselt, K. A., Landolt, A. U., & Wolff, M. J. 2003, *ApJ*, 594, 279
- Graczyk, D., Pietrzyński, G., Thompson, I. B., et al. 2020, *ApJ*, 904, 13
- Guinan, E. F., Fitzpatrick, E. L., DeWarf, L. E., et al. 1998, *ApJL*, 509, L21
- Hubble, E. 1929, *Proceedings of the National Academy of Science*, 15, 168
- Inno, L., Matsunaga, N., Romaniello, M., et al. 2015, *A&A*, 576, A30
- Jacyszyn-Dobrzeńicka, A. M., Skowron, D. M., Mróz, P., et al. 2016, *AcA*, 66, 149
- Kodric, M., Riffeser, A., Hopp, U., et al. 2018, *AJ*, 156, 130
- Leavitt, H. S., & Pickering, E. C. 1912, *Harvard College Observatory Circular*, 173, 1
- Lemasle, B., Groenewegen, M. A. T., Grebel, E. K., et al. 2017, *A&A*, 608, A85
- Li, S., Riess, A. G., Busch, M. P., et al. 2021, *ApJ*, 920, 84
- Lindgren, L., Bastian, U., Biermann, M., et al. 2021, *A&A*, 649, A4
- Luck, R. E., & Lambert, D. L. 2011, *AJ*, 142, 136
- Madore, B. F., & Freedman, W. L. 2024, *ApJ*, 961, 166



- Mathewson, D. S., Ford, V. L., & Visvanathan, N. 1988, *ApJ*, 333, 617
- Momcheva, I. G., van Dokkum, P. G., van der Wel, A., et al. 2017, *PASP*, 129, 015004
- Murakami, Y. S., Riess, A. G., Stahl, B. E., et al. 2023, *JCAP*, 2023, 046
- Murray, C. E., Hasselquist, S., Peek, J. E. G., et al. 2024, *ApJ*, 962, 120
- Nidever, D. L., Monachesi, A., Bell, E. F., et al. 2013, *ApJ*, 779, 145
- Owens, K. A., Freedman, W. L., Madore, B. F., & Lee, A. J. 2022, *ApJ*, 927, 8
- Pietrzyński, G., Graczyk, D., Gallenne, A., et al. 2019, *Nature*, 567, 200
- Planck Collaboration, Aghanim, N., Akrami, Y., et al. 2020, *A&A*, 641, A6
- Reid, M. J., Pesce, D. W., & Riess, A. G. 2019, *ApJL*, 886, L27
- Riess, A. G., Casertano, S., Yuan, W., et al. 2021, *ApJL*, 908, L6
- Riess, A. G., Casertano, S., Yuan, W., Macri, L. M., & Scolnic, D. 2019a, *ApJ*, 876, 85
- Riess, A. G., Narayan, G., & Calamida, A. 2019b, Calibration of the WFC3-IR Count-rate Nonlinearity, Sub-percent Accuracy for a Factor of a Million in Flux, Tech. rep., STScI
- Riess, A. G., Casertano, S., Yuan, W., et al. 2018, *ApJ*, 855, 136
- Riess, A. G., Yuan, W., Macri, L. M., et al. 2022a, *ApJL*, 934, L7
- Riess, A. G., Breuval, L., Yuan, W., et al. 2022b, *ApJ*, 938, 36
- Ripepi, V., Cioni, M.-R. L., Moretti, M. I., et al. 2017, *MNRAS*, 472, 808
- Ripepi, V., Catanzaro, G., Clementini, G., et al. 2022, *A&A*, 659, A167
- Ripepi, V., Clementini, G., Molinaro, R., et al. 2023, *A&A*, 674, A17
- Romaniello, M., Riess, A., Mancino, S., et al. 2022, *A&A*, 658, A29
- Sahu, K., Baggett, S., & MacKenty, J. 2014, Use of the Shutter Blade Side for UVIS Short Exposures, Instrument Science Report WFC3 2014-009, 16 pages
- Sakai, S., Ferrarese, L., Kennicutt, Robert C., J., & Saha, A. 2004, *ApJ*, 608, 42
- Sandage, A., Tammann, G. A., & Reindl, B. 2009, *A&A*, 493, 471
- Scowcroft, V., Freedman, W. L., Madore, B. F., et al. 2016, *ApJ*, 816, 49
- Soszyński, I., Udalski, A., Szymański, M. K., et al. 2015, *AcA*, 65, 297
- Taormina, M., Kudritzki, R.-P., Puls, J., et al. 2020, *ApJ*, 890, 137
- Trentin, E., Ripepi, V., Molinaro, R., et al. 2024, *A&A*, 681, A65
- Urbaneja, M. A., Kudritzki, R.-P., Bresolin, F., et al. 2008, *ApJ*, 684, 118
- Verde, L., Schöneberg, N., & Gil-Marín, H. 2023, arXiv e-prints, arXiv:2311.13305
- Wielgórski, P., Pietrzyński, G., Gieren, W., et al. 2017, *ApJ*, 842, 116
- Wu, J., Scolnic, D., Riess, A. G., et al. 2023, *ApJ*, 954, 87